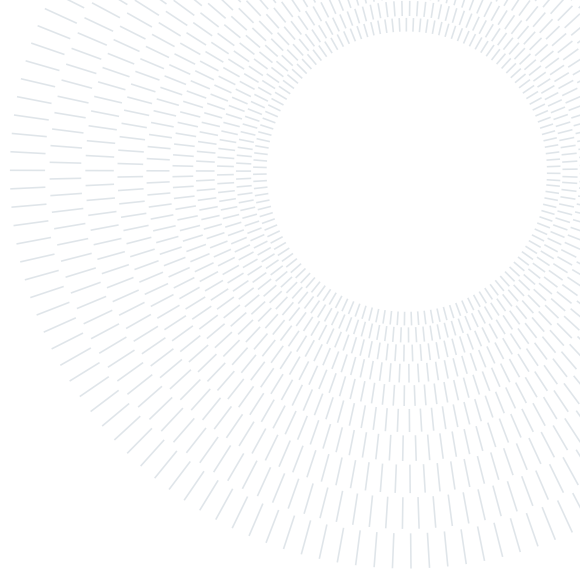




**POLITECNICO**  
MILANO 1863

SCUOLA DI INGEGNERIA INDUSTRIALE  
E DELL'INFORMAZIONE



#### EXECUTIVE SUMMARY OF THE THESIS

## Synchrotron-Based Study of Lithium-ion Battery Failure: Pipeline for Agglomerate Segmentation and Analysis

LAUREA MAGISTRALE IN PHYSICS ENGINEERING - INGEGNERIA FISICA

**Author:** MATTEO VENTURELLI

**Advisor:** PROF. GIACOMO CLAUDIO GHIRINGHELLI

**Co-advisors:** MATILDA FRANSSON, LUDOVIC BROCHE

**Academic year:** 2022-2023

---

## 1. Introduction

Addressing climate change, underscored by rising CO<sub>2</sub> emissions, is crucial, especially within the high-emission transportation sector. The shift towards electric vehicles, powered by lithium-ion batteries (LIBs), presents a sustainable solution. LIBs offer advantages like high energy density and lower environmental impact, making them key to reducing emissions. However, they face challenges like thermal runaway (TR), a catastrophic failure mode not fully understood in existing literature.

This work aims to provide novel insights into TR dynamics using high-speed X-ray imaging at the European Synchrotron's ID19 beamline, in collaboration with the Fraunhofer Institute for High-Speed Dynamics (EMI) and University College London (UCL). The focus is on post-processing and analyzing high-speed tomography data to segment, characterize and visualize agglomerates formed inside batteries during TR. This research is significant in its potential to contribute to the understanding of LIBs failure mechanisms, thereby guiding battery designers and manufacturers in developing safer batteries and effective mitigation systems.

## 2. Lithium-ion Batteries and Abuse Testing

A lithium-ion battery consists of two electrodes, an electrolyte, a separator, two current collectors and a metal casing. The positive and negative electrode materials are powders that are applied as coatings on current collector foils, resulting in composite electrodes. The ion-conducting electrolyte and the separator, an electrolyte-permeable membrane to electrically isolate the two electrodes, are situated between the two electrodes. The electrolyte facilitates the movement of lithium ions while compelling electrons to travel through an external circuit to perform work. Metallic current collectors deliver electronic current from/to the redox centers of the electrodes to/from the external circuit [1]. These elements are used to produce cylindrical, prismatic and pouch cells. Depending on the application, a single battery cell could be used or several cells could be connected either in series or parallel, forming a module. Several connected modules form a battery system for auto-motive applications.

## 2.1. Battery Failure and Safety Tests

Rising battery temperature under extreme conditions could trigger undesirable reactions, causing TR, where battery heat generation cannot be controlled. Generally, TR occurs when the heat generated by exothermic reactions is not offset by the heat losses to the environment. This accumulated heat drives the temperature increase which, in turn, produces an exponential increase in the reaction rates. If the rate of heat generation exceeds the rate of heat dissipation into the environment, the temperature will continue rising. When reaching some critical temperatures, especially the collapse temperature of separator, the cell will breakdown [2].

Stringent safety standards and corresponding assessments have been established to minimize the likelihood of safety issues in routine working conditions and ensure that batteries available on the market are of sufficient quality for intended purposes. In a safety test, possible trigger modes are simplified so batteries TR characteristics are measurable in the laboratory. The tests are designed to simulate the most severe conditions that a battery could face during its life cycle, including internal short circuit, nail penetration, and external heating [2].

## 2.2. Phase Contrast X-ray CT

At the European Synchrotron, high-speed phase contrast X-ray CT was employed for the first time to capture the dynamic processes occurring within LIBs during abuse tests [3]. This technique provides a unique capability to visualize the internal structure of LIBs at high temporal and spatial resolutions, providing a completely new perspective on the TR process.

X-ray computed tomography (CT) utilizes X-rays' ability to penetrate objects, capturing multiple two-dimensional radiographs from various angles. These radiographs are then processed through a reconstruction algorithm to produce a digital greyscale three-dimensional image, showcasing the internal structure of the object. This 3D representation allows for detailed analysis and virtual manipulation, including slicing in any direction and enhancing specific features for better visualization.

## 2.3. Experimental Setup

The battery abuse tests described herein were conducted during the July 2022 beamtime at the synchrotron, prior to the commencement of this thesis. My role involved analyzing the data obtained from these experiments to gain insights into TR dynamics and agglomerate formation within LIBs.

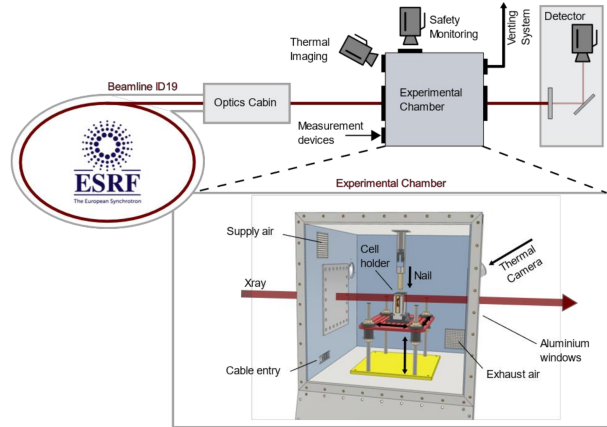


Figure 1: Schematic of the experimental setup for battery abuse testing.

To perform battery abuse test at the synchrotron, a specialized X-ray penetrable chamber [4] has been developed and installed at the beamline (Figure 1). The chamber provides the capability to robustly perform *in situ* abuse tests through the heat-resistant and gas-tight design for flexible battery geometries and configurations. The chamber is equipped with a high-speed sample rotation stage (20 Hz) and compatible sample holders for different battery types. The X-ray CT setup is complemented by a high-speed Photron SA-Z CMOS camera and a 1000  $\mu\text{m}$ -thick LuAG:Ce scintillator, allowing for the acquisition of 30000 projections per second. Three different TR initiation modes (nail penetration, external heating, and internal short circuit device) were employed in this work. Two battery models, Molicel INR-18650-P28A 2800 mAh (P28A) and Sony Murata US-18650-VTC5A 2600 mAh (VCT5A), were each subjected to nail penetration and external heating, whereas Molicel INR-18650-P28B 2800 mAh (P28B) was subjected to ISC. The data was acquired as 12-bit greyscale TIFF 1024 $\times$ 512 images, then cropped to 640 $\times$ 280 due to the limited beam size in the vertical direction and limited battery size in the horizontal direction (al-

lowing for  $25.6 \times 11.2$  mm FoV with  $40 \mu\text{m}$  pixel size). The  $640 \times 640 \times 280$  volumes were reconstructed and converted from TIFF file collections to NumPy volumes for further analysis.

### 3. Developed Software

A preliminary analysis of the reconstructed volumes has highlighted agglomerate formation as a critical event during TR. These agglomerates originate from battery materials melting as a consequence of the intense heat generation during failure. A systematic agglomerate study is essential to understand the TR process and its implications for battery safety. To this end, a software pipeline has been developed to segment and analyze agglomerates in the reconstructed volumes [5]. The pipeline is implemented in Python and is composed of three main modules: (1) segmentation, (2) feature extraction, and (3) visualization.

#### 3.1. Segmentation

The segmentation algorithm developed for this study, outlined in Algorithm 1, integrates thresholding, morphological operations, and filtering techniques.

**Algorithm 1** Segmentation algorithm outline.

---

```

1: Compute threshold
2: Segment ct[0]
3: i = 1
4: while i < T do
5:   Segment ct[i]
6:   Propagate labels from mask[i-1] to
      mask[i]
7:   i = i + 1
8: end while
9: Filter mask
```

---

Input **ct** is a NumPy array of reconstructed volumes with the shape (223, 280, 640, 640), corresponding to the dimensions (**t**, **z**, **y**, **x**). The number **T** of reconstructed volumes per experiment is 223, and each volume comprises  $640 \times 640 \times 280$  voxels.

Output **mask** is a NumPy array of the same shape as **ct**, containing a multi-label map. Here, 0 denotes the background, 1 indicates the battery casing and integers greater than 1 identify copper agglomerates.

Initially, the algorithm calculates a threshold

value for segmenting the volumes **ct**[**i**]. Using this threshold, the first volume is segmented to produce an initial label map **mask**[0]. For subsequent volumes **ct**[**i**], the algorithm computes **mask**[**i**] and propagates labels from **mask**[**i**-1] to ensure continuity of agglomerate identification across volumes. The final step involves applying filtering techniques to the label map to refine segmentation quality and eliminate artifacts.

#### 3.2. Feature Extraction

The label map constructed by the segmentation algorithm serves as the foundation for extracting a range of agglomerates morphological and spatial features, including position, volume and velocity. These features are used to draw plots and visualize the agglomerates' evolution over time in different regions of the battery. Examples are shown in Figure 3 and 4.

#### 3.3. Visualization

The visualization module is designed to provide a comprehensive view of the agglomerates' evolution over time. 2D visualization was achieved by the integration of the **napari** viewer into the pipeline, allowing for interactive exploration of the segmentation maps overlaid directly onto the reconstructed volumes. For comprehensive 3D visualization, Blender was utilized to render volumetric representations of the segmented features. A custom algorithm was developed to convert the segmentation maps into **STL** files, enabling a detailed rendering of 3D volumes for each experiment. Examples can be found both in Figure 2 and in the GitHub repository [5].

### 4. Results

The developed software pipeline was applied to the reconstructed volumes from the battery abuse tests. The results provide a detailed examination of agglomerate formation during TR, offering insights into the dynamics and heat distribution of the failure process.

#### 4.1. Initiation Method Comparison

Valuable insights emerge from examining the agglomerate features plots and the renderings. Notably, for the **heat** initiation method, agglomerates are observed to form initially in the outermost part of the battery, moving gradually

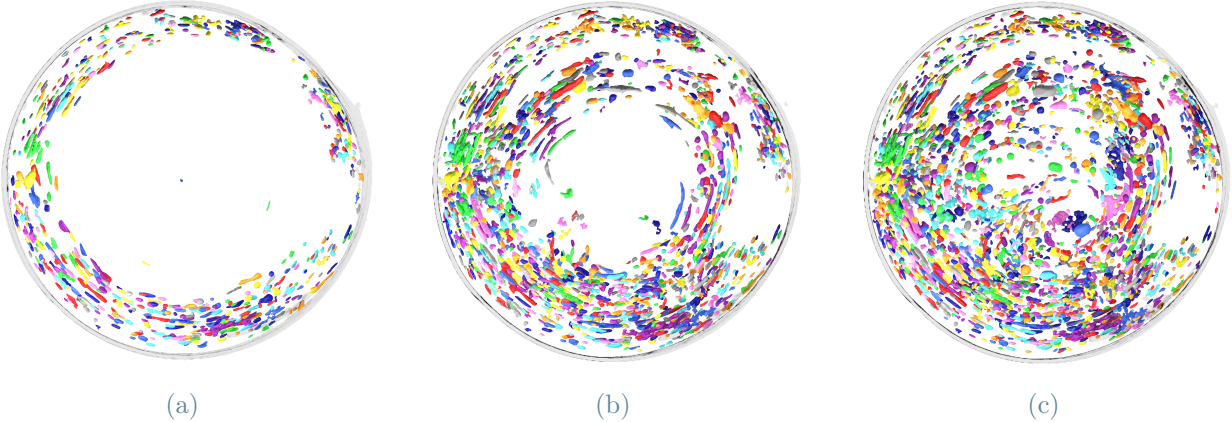


**Figure 2:** P28A\_Heat\_Exp4\_2: Agglomerate renderings (top view) after 0.5 (a), 1.4 (b) and 2.3 s (c) from the start of the thermal runaway.

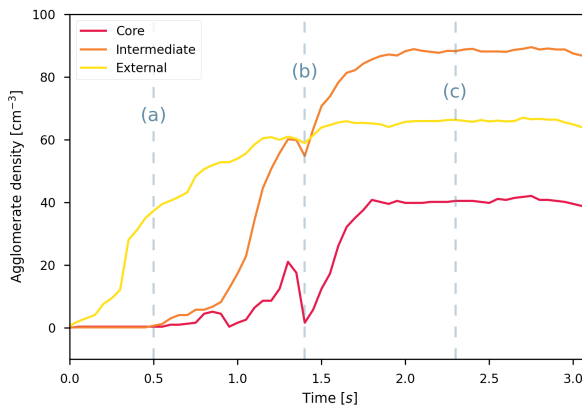


**Figure 3:** P28A\_Heat\_Exp4\_2: Plot of the agglomerate density as a function of time for the three radial sections of the battery. Agglomerate density increases first in the outermost section (a), followed by the middle section (b) and the innermost section (c). Renderings related to (a), (b) and (c) are shown in Figure 2a, 2b and 2c, respectively.

towards the center. This pattern likely results from the heat gun's focus on the casing, creating a temperature gradient where the temperature is lower in the center. This gradient facilitates the melting of metals close to the battery casing, with a gradual progression towards the center as the heat diffuses inward. This phenomenon, illustrated in Figures 2 and 3 for P28A, is apparent in both battery types, despite it being less distinct in VCT5A.

In contrast, the **nail** initiation method exhibits an opposite trend, illustrated in Figure 4, with agglomerates forming centrally and spreading towards the casing, attributed to the nail's pen-

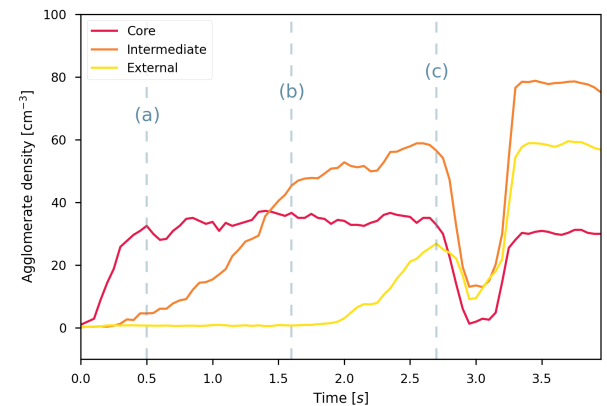


**Figure 4:** VCT5A\_Nail\_Exp4: Plot of the agglomerate density as a function of time for the three radial sections of the battery. Agglomerate density increases first in the innermost section (a), followed by the middle section (b) and finally the outermost section (c).

etration along the battery's axis.

**ISC** experiments displayed markedly violent battery failures, likely due to the rapid heat release characteristic of the internal short circuit initiation method. Sidewall rupture occurred in each of the experiments, facilitating heat and mass exchange with the environment, likely preventing the conditions necessary for agglomerate formation to be met.

#### 4.2. P28A - VCT5A Comparison

The boxplots in Figure 5 show the total agglomerate volume, average agglomerate volume and agglomerate density for each battery type. It was observed that VCT5A batteries exhibit a higher total agglomerate volume and average ag-

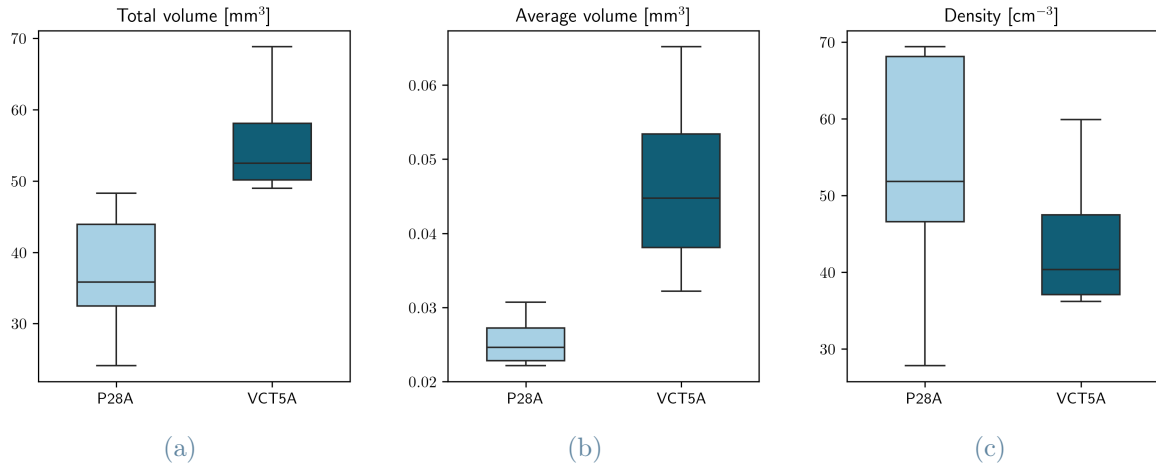


**Figure 5:** Boxplots for total agglomerate volume **(a)**, average agglomerate volume **(b)** and agglomerate density **(c)**, comparing P28A and VCT5A battery types.

glomerate volume, while P28A batteries show a slightly higher agglomerate density (Figure 5). It's noted that boxplot 5b uses the average agglomerate volume per experiment for comparison, which may not fully capture the variability seen when considering each agglomerate's volume individually. This variability is illustrated in the agglomerate size plots in Figure 6, where a longer tail is observed for VCT5A batteries, indicating a higher number of large agglomerates.

To statistically validate the observed differences in agglomerate volume distribution between the two battery types, the application of the ANOVA and Welch statistical tests is proposed, aiming to demonstrate a significant difference in the mean values of the two distributions. One-way ANOVA was initially applied, yielding an F-statistic of approximately  $2.72 \cdot 10^2$  and a highly significant p-value ( $3.60 \cdot 10^{-60}$ ), suggesting significant differences between the groups. However, given the underlying assumptions of normality and homogeneity of variances (homoscedasticity) associated with ANOVA, which the data violated, a more robust test was employed. Welch's t-test, better suited for datasets that do not meet these assumptions, was then conducted. It produced a t-statistic of  $-1.14 \cdot 10^1$  and a highly significant p-value ( $4.09 \cdot 10^{-29}$ ), conclusively indicating a significant difference in mean agglomerate volumes between P28A and VCT5A batteries, reinforcing the initial ANOVA findings under more relaxed assumptions regarding data distribution and variance.

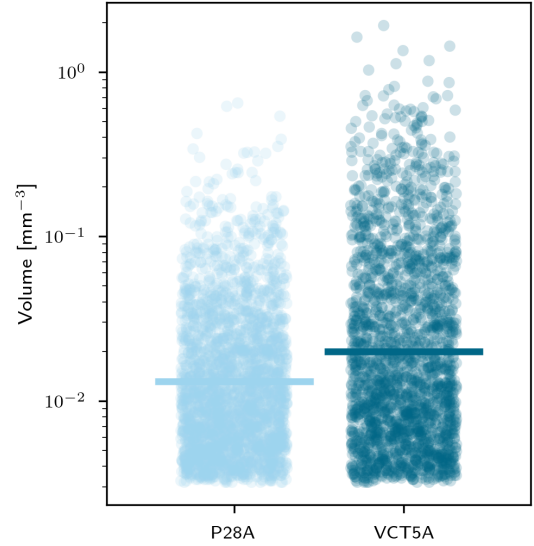


**Figure 6:** Agglomerate size point plot in logarithmic scale for P28A and VCT5A battery types (solid lines indicate the average agglomerate volume).

Following the observed differences in agglomerate volumes between the two battery types, a supplementary experiment was conducted to measure the thickness of Cu current collector for comparison purposes. The focus on Cu, as opposed to other battery materials, is due to its highly attenuating nature, resembling agglomerates in the reconstructed volumes.

The setup for high-resolution tomography was configured to achieve a pixel size of  $0.65 \mu\text{m}$ , utilizing a  $25 \mu\text{m}$ -thin LuAG:Ce scintillator coupled

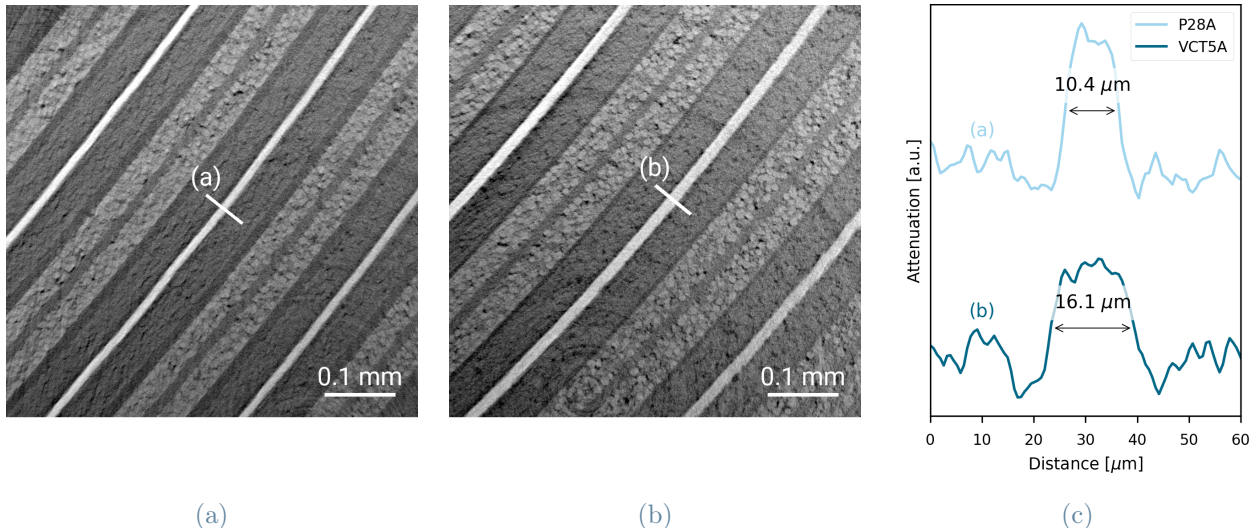


**Figure 7:** High resolution CT slices for P28A (a) and VCT5A (b) batteries. The profile plot (c) shows the copper current collector thickness for the two battery types.

with a pco.edge sCMOS camera and a  $10\times$  Mitutoyo lens. The Cu current collector in VCT5A batteries was found to be over 50% thicker than that in P28A batteries (Figure 7), providing a potential explanation for the denser agglomerate formation observed in VCT5A batteries.

## 5. Conclusions

This work showcases the significant advancement in battery research through the development of an image processing pipeline at ESRF, highlighting its role in understanding thermal runaway in lithium-ion batteries by providing a detailed examination of agglomerate formation. Future directions could include leveraging the findings of this research as validation for simulations, enhancing the segmentation process for improved accuracy, and investigating the chemical composition of agglomerates using EDX. This foundational framework supports further research, promising enhanced battery safety and performance insights.

## References

- [1] Reiner Korthauer, ed. *Lithium-Ion Batteries: Basics and Applications*. Trans. by Michael Wuest. Berlin [Heidelberg]: Springer, 2018.
- [2] Qingsong Wang et al. “Thermal Runaway Caused Fire and Explosion of Lithium Ion Battery”. In: *Journal of Power Sources* 208 (June 2012), pp. 210–224.
- [3] Donal P. Finegan et al. “In-Operando High-Speed Tomography of Lithium-Ion Batteries during Thermal Runaway”. In: *Nature Communications* 6.1 (Apr. 2015), p. 6924.
- [4] J. Pfaff et al. “In Situ Chamber for Studying Battery Failure Using High-Speed Synchrotron Radiography”. In: *Journal of Synchrotron Radiation* 30.1 (Jan. 2023), pp. 192–199.
- [5] Matteo Venturelli. *Fasttomo Repository*. <https://github.com/venturellimatteo/fasttomo>. Feb. 2024.